Supplementary Information (SI) for Energy & Environmental Science.
This journal is © The Royal Society of Chemistry 2026

Supplementary Information

Towards Space Compatible Perovskite Solar Cells: Guidelines for Thermal Shock Resilience and Near Space Balloon Testing

Minwoo Lee[1,†], George Kwesi Asare[2,3,†], Tommy Richards[4], Dong Gyu Lee[5], Tae Kyung Lee[5,6], Jongsung Park[7], Juhong Oh[8], Jihoo Lim[1], Martin A. Green[1], Xiaojing Hao[1,*], Dohyung Kim[9,10,*], Helen Hejin Park[2,3,*], and Jae Sung Yun[1,4,*]

[1]Australian Centre for Advanced Photovoltaics (ACAP), School of Photovoltaic and Renewable Energy Engineering, University of New South Wales, Sydney, NSW 2052, Australia

[2]Advanced Materials Division, Korea Research Institute of Chemical Technology (KRICT), Daejeon, 34114, Republic of Korea

[3]Department of Advanced Materials and Chemical Engineering, University of Science and Technology (UST), Daejeon, 34113, Republic of Korea

[4]Department of Electrical and Electronic Engineering, Advanced Technology Institute (ATI), University of Surrey, Guildford, Surrey GU2 7XH, United Kingdom

[5]Department of Materials Engineering and Convergence Technology, Gyeongsang National University, Jinju, 52828, Republic of Korea

[6]School of Materials Science and Engineering, Gyeongsang National University, Jinju, 52828, Republic of Korea

[7]Department of Energy Engineering, Future Convergence Technology Research Institute, Gyeongsang National University, Jinju, 52828, Republic of Korea

[8]Korea Testing Laboratory (KTL) Space Testing Center, 16, Sangdae-ro 72 beon-gil, Jinju-si, Gyeongsangnam-do, 52852, Republic of Korea

[9]Department of Advanced Materials Engineering, Chungbuk National University, Cheongju, 28644, Republic of Korea

[10]Department of Urban, Energy, Environment Engineering, Chungbuk National University, Cheongju, 28644, Republic of Korea

*Corresponding authors: xj.hao@unsw.edu.au, dohyungkim@chungbuk.ac.kr, hhpark@krict.re.kr, j.yun@surrey.ac.uk

†These authors contributed equally to this work.

Methodology

Materials:

Materials

ITO glass substrate with ITO thickness of 100 nm was purchased from AMG. Nano-particle tin (IV) oxide (NP-SnO_2) was prepared from Sukgyung Gel solution. Formamidinium iodide ($FAPbI_3$) and methylammonium bromide ($MAPbBr_3$) were prepared at KRICT (Perovskite department group). Methylammonium chloride (MACl, ≥ 98%), N, N-dimethylformamide (DMF, 99.8%), dimethyl sulfoxide (DMSO, 99.9%), toluene (99.8%), phenylenthylammonium iodide (PEAI), and cerium oxide (CeOx, ≥ 25nm particle size) were purchased from Sigma-Aldrich. Poly(triarylamine) (molecular weight average (Mw): 110 kDa) was purchased from MS solution. Octylammonium bis(trifluoromethylsulfonyl)imide (OATFSI) was synthesized at KRICT, and ethylacetate (EA, 99.0%) was purchased from Duksan Pure Chemicals. All purchased chemicals were used without any additional processing.

Device Fabrication

For the fabrication of perovskite solar cell unit cells, ITO glass substrates were systematically washed in deionized water (DI), acetone, and isopropyl alcohol respectively for 15 minutes during each washing process. After washing, ITO glass substrates were dried in a 100 ℃ oven for 5 minutes to ensure thorough drying. NP-SnO_2 was prepared by mixing sukgyung gel SnO_2 solution and deionized water in the ratio 1:5 respectively. The resulting solution was spin coated onto the ITO/Glass substrate at 3000 rpm for 30 seconds, followed by annealing of the substrates on a hotplate at 150°C for 30 minutes. The reference perovskite precursor solution (0% $MAPbBr_3$) was synthesized by dissolving 800 mg of $FAPbI_3$ and 40 mg of MACl in a mixed solvent of DMF/DMSO (in a ratio of 8:1 v/v). For the variation of $MAPbBr_3$ concentrations, mole fractions of 6.05 mg, 18.16 mg, 30.27 mg, and 42.37 mg representing 1%, 3%, 5%, and 7% $MAPbBr_3$ respectively, were added to 800 mg $FAPbI_3$ and 30 mg of MACl in a mixed solvent of DMF/DMSO (in a ratio of 8:1 v/v). The resulting perovskite precursor solutions were spin-coated onto the np-SnO_2/ITO/Glass substrate at 500 rpm for 5 seconds, 1000 rpm for 8 seconds, and 5000 rpm for 12 seconds. During the final state, ethyl acetate anti-solvent was dripped onto the perovskite precursor at 12 s followed by annealing at 100°C for 1 hour and then 150°C for 4 minutes respectively. PEAI passivation solution was spin coated on top of the perovskite film at 5000 rpm for 30 seconds. PTAA solution was prepared by dissolving 0.01g PTAA in toluene and OATFSI additive added after which resulting solution spin coated onto the perovskite passivated film surface at 3000 rpm for 30 seconds. Finally, a gold (Au) top electrode was deposited by thermal evaporator with a power of 0.98 W on top of the PTAA layer to complete the full perovskite solar cell devices. The perovskite solar cells were encapsulated by PIB tape with full cover for the balloon test.

Evaluation and characterisation

Thermal shock test

Thermal shock test was conducted using the TS-60 thermal shock test chamber by Weiss technik. This shock test method is conducted to determine the resistance of a semiconductor device to extremes of high and low temperatures, and to the effect of alternate exposures to these extremes. The test conditions were -80 degrees for low temperature and 80 degrees for high temperature, exposure for 15 minutes, repeated 100 times.

Calculation of temperature rate vs altitude

Used the temperature rate calculation as below;

$$\frac{dT}{dt} = \frac{\Delta T}{\Delta t}$$

where:

- dT/dt is the temperature change rate (°C/min),
- ΔT is the temperature difference 80−(−80) = 160 °C,
- Δt is the duration of the respective phase (eclipse or sunlight) for a circular orbit at altitudes from 200 km to 2000 km.

The temperature rates for the cooling and heating phases differ due to the geometric asymmetry of the orbital cycle. In Low Earth Orbit (LEO), the satellite traverses the Earth's shadow (eclipse phase) for a significantly shorter duration (~35–37 min) compared to the sunlight phase (~51–92 min). Since the total temperature variation (ΔT = 160 °C) is constant for both transitions, the cooling process occurs more rapidly, resulting in a higher temperature rate during the eclipse compared to the sunlight phase.

Standard of thermal cycle IEC 61215

The test involves cycling the temperature between -40 ℃ and +85 ℃ in a controlled chamber, with specific ramp rates and dwell times [1]:

where:

- Lower limit: -40 ℃
- Upper limit: +85 ℃
- Cycle duration: Typically 3–4 hours per cycle
- Number of cycles: 200 cycles for full qualification
- Dwell time: A minimum of 10 minutes at each extreme temperature

The thermal cycling test simulates day-night temperature fluctuations and extreme environmental conditions that PV modules experience over their lifetime.

Density functional theory (DFT)-based molecular dynamics (MD) simulation

We performed DFT-based MD simulations to investigate the structural properties of $FAPbI_3$ perovskite by using the Cambridge Serial Total Energy Package program[2]. The generalized gradient approximation with Perdew-Burke-Ernzerhof functional[3] was used for the exchange-correlation energy with the spin polarization. Ultrasoft and Tkatchenko and Scheffler method[4] were adopted for pseudopotential and dispersion correction, respectively. The value of energy cut-off was set to 240 eV. The k-points[5] were set to 4 × 4 × 4 for 2 × 2 × 2 supercell system of $FAPbI_3$ unit cell. The calculation of self-consistent field was set to 2×10^{-6} eV/atom. For the DFT-based MD simulations, the NPT ensemble (i.e., isothermal-isobaric ensemble, P = 1 atm and T = -80 °C, 25 °C, or 80 °C) was performed for 0.5 ps using Nosé-Hoover thermostat and Parrinello-Rahman barostat with a time step of 1 fs.

X-ray diffraction (XRD)

XRD patterns were measured using a PANalytical Xpert Materials Research diffractometer system with a Cu Kα radiation source (λ = 0.1541 nm) at 45 kV and 40 mA.

Scanning electron microscopy (SEM)

SEM was carried out using a Nova Nano 230 instrument, using a 5 kV accelerating voltage and a 10 µs dwell time.

Spectral photoluminescence (SSPL) measurement

PL was measured using a time-correlated single-photon counting method using commercial equipment (FluoTime 250, PicoQuant) equipped with a 470 nm excitation source and a 500 nm long pass filter. The samples were excited through the perovskite film surface.

Kelvin probe force microscopy (KPFM) measurement

KPFM measurements were performed by using NX-10 Park Systems in an ambient atmosphere. The data were acquired by using a radius of curvature of 35 nm (HA_NC/Au) cantilever and k = 3.5 ± 20% n/m. The scan rate was 0.25 Hz and performed at 1.5 µm at 256 pixels. Sideband KPFM was utilized with the sideband's frequency of 3 kHz instead of 17 kHz. The KPFM data was analysed by Gwyddion.

J-V measurement

Illuminated J-V characteristics were measured using a Keithley 2420 sourcemeter. The standard 100 mW/cm^2 (1 SUN) illumination was generated by a Newport Oriel Class A 91195A solar simulator using a 450 W Xe-lamp (Oriel) with an AM 1.5G filter, while the light intensity was calibrated by a Si-reference cell certified by NREL. The J-V curves were measured from 1.5 V to -0.2 V along the reverse scan and forward scan directions, with a step voltage and scan speed fixed at 10 mV and 150 mV/s, respectively and the delay time was fixed at 10 ms. All devices were measured with a shadow mask with an active area of 0.094 cm^2.

External quantum efficiency measurement (EQE)

Newport Quantx-300 was used to measure the device's EQE. The system was firstly calibrated from 300 nm - 850 nm wavelength range at each 10 nm step to provide spectral resolution. The perovskite device was set up in the Quantx-300 system's sample holder after calibration. The incident photon flux at each wavelength was measured using a reference detector, a calibrated silicon photodiode. The broadband light was produced by a Xenon arc lamp and was distributed by a monochromator to isolate specific wavelengths for the EQE measurement. The lock-in amplifier was utilized to measure the device's photocurrent response while maintaining synchronization with the optical chopper frequency of 94.6 Hz.

High altitude balloon test (HAB)

A helium-filled latex balloon carried a payload gondola built on the UniPiHAB platform. four perovskite solar cells were mounted on the external panel; each device was measured 127 times using forward-only I–V scans (127 I–V curves per device, 381 total). During shipment the cells were sealed in vacuum bags. On site it was affixed to the gondola panel and briefly illuminated with a 50 W lamp to verify electrical connections and data logging. Details of the measurement circuit are provided elsewhere[6]. After assembly the perovskite solar cells were kept covered and stored at room temperature for 48 h prior to flight. At the launch site a "Weather Balloon 1600" was filled with helium. Immediately before launch the cell cover was removed, and the balloon was released at 15:00 local time. The flight lasted approximately 2 h 20 min to a peak altitude of ~35 km. Each measurement cycle used a capacitor-charging method to sweep the device voltage; one cycle took ~52 s. During each cycle, temperature and irradiance were recorded while the capacitor was charged by the test cell. A 16-bit ADC measured the current and the voltage drop across a shunt resistor, from which I–V curves were reconstructed. Since, the sweep was driven by the charging capacitor, the voltage range and effective scan rate varied with irradiance and device current. Due to system limitations described in the literature[6], the first data point did not reach a strictly open-circuit condition; given the small slope near open circuit, the first point was treated as an approximation of V_{OC}. Only forward (increasing-voltage) scans were performed, so hysteresis could not be assessed.

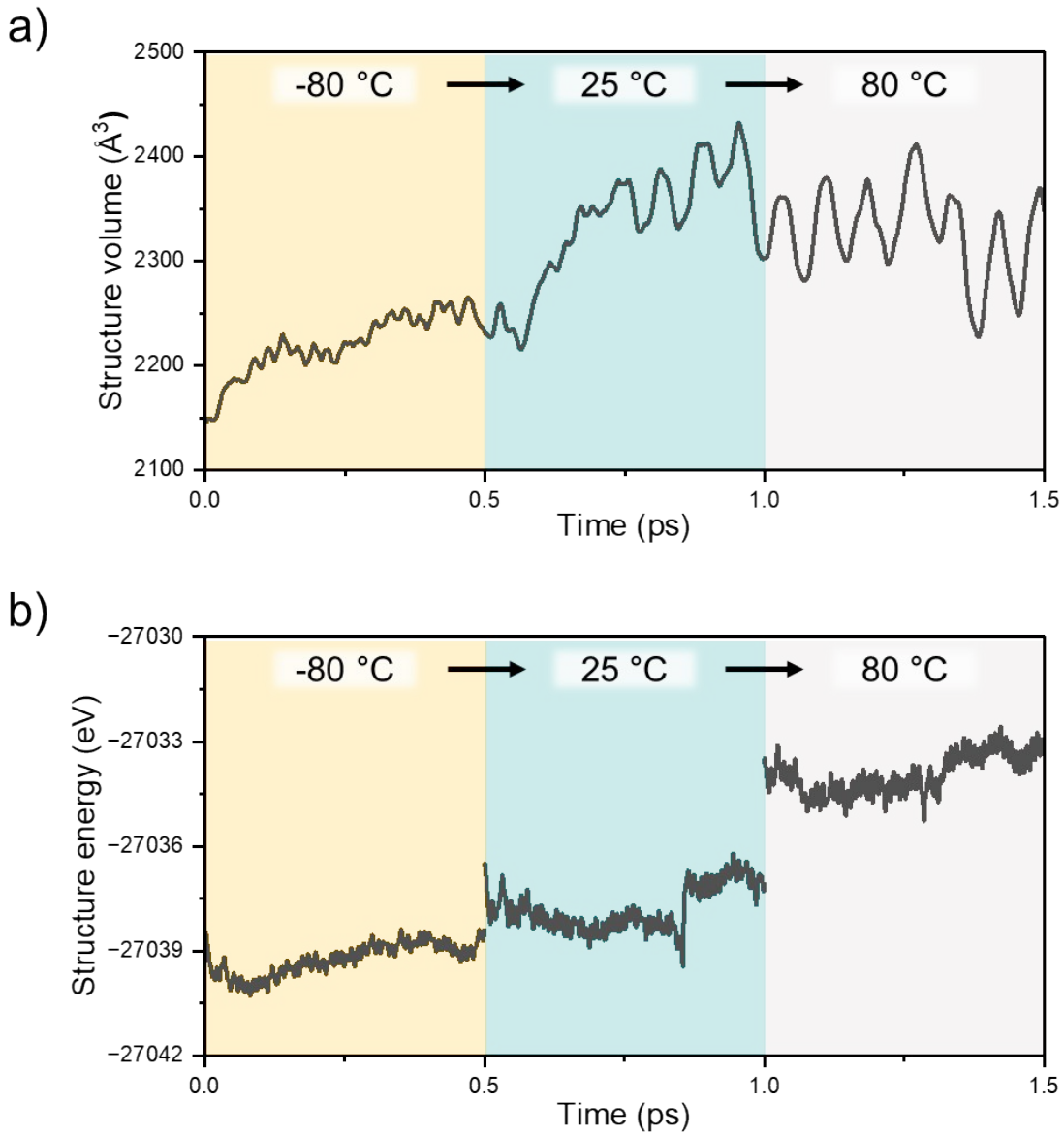

Figure S1. Changes of structure volume and energy of $FAPbI_3$ according to temperature condition and simulation time.

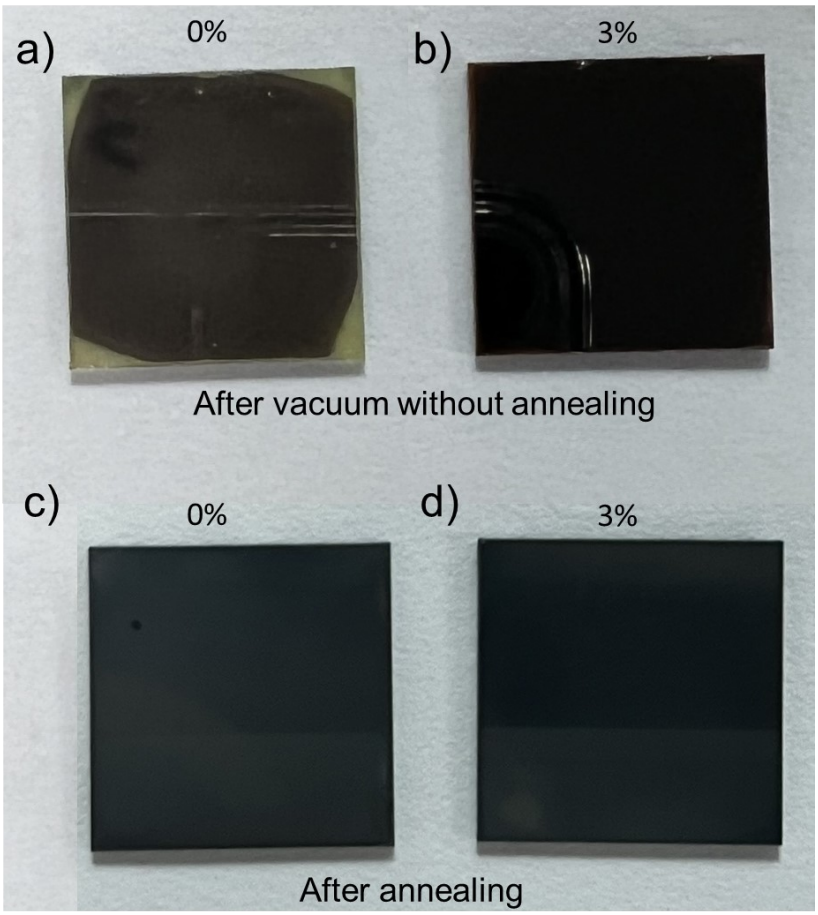

Figure S2. Perovskite films prepared with and without annealing treatment after spin coating: (a) 0% $MAPbBr_3$ under vacuum conditions without annealing, (b) 3% $MAPbBr_3$ under vacuum conditions without annealing, (c) 0% $MAPbBr_3$ after annealing, and (d) 3% $MAPbBr_3$ after annealing.

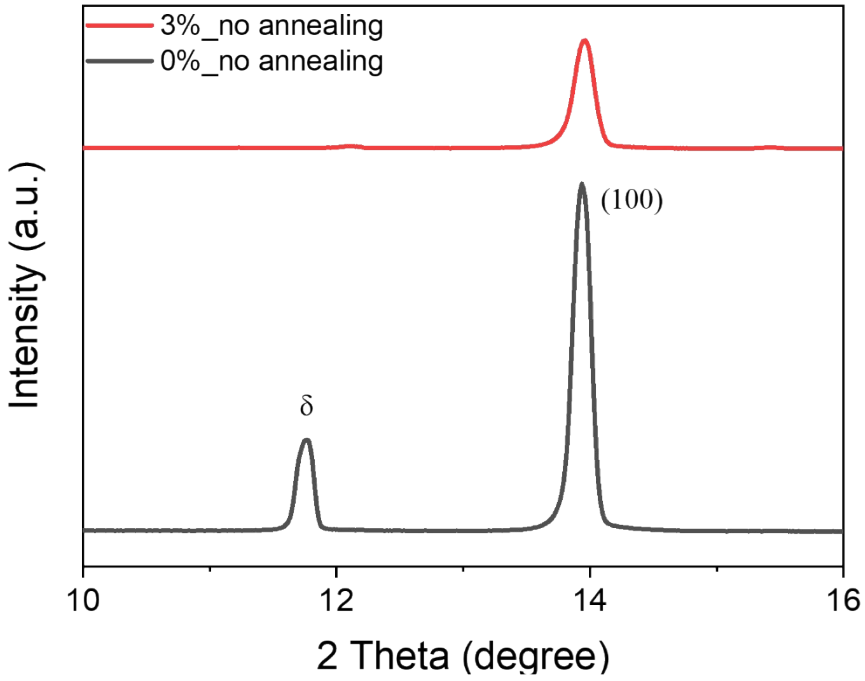

Figure S3. XRD patterns of perovskite films containing 0% and 3% $MAPbBr_3$, dried under vacuum conditions.

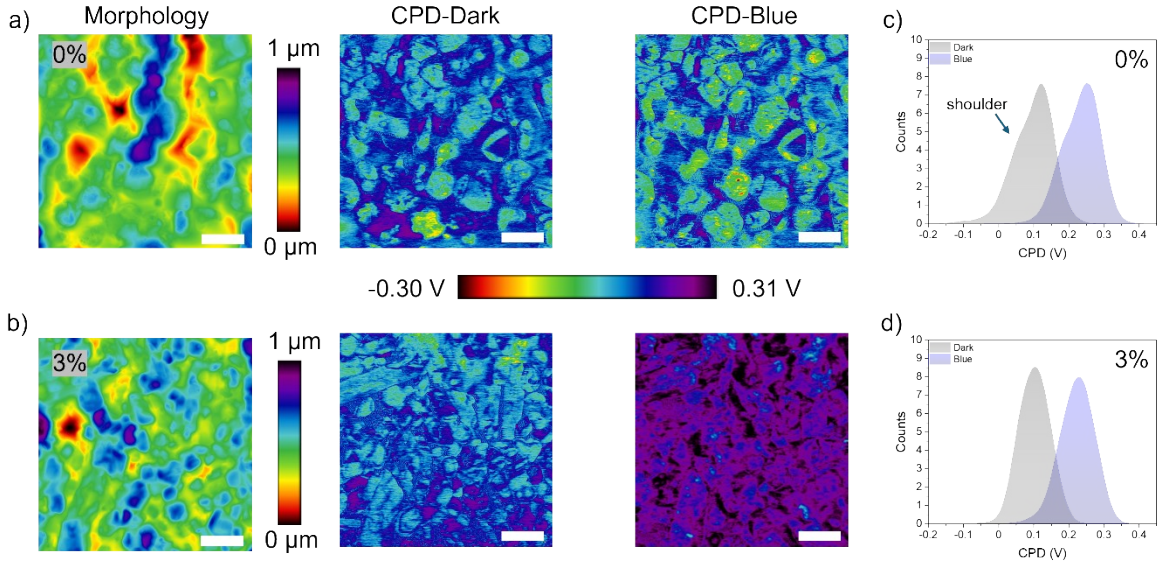

Figure S4. Morphology KPFM images of perovskite films with 0% (a) and 3% (b) $MAPbBr_3$ under dark and blue-illumination conditions. The scale bar corresponds to 1 µm.

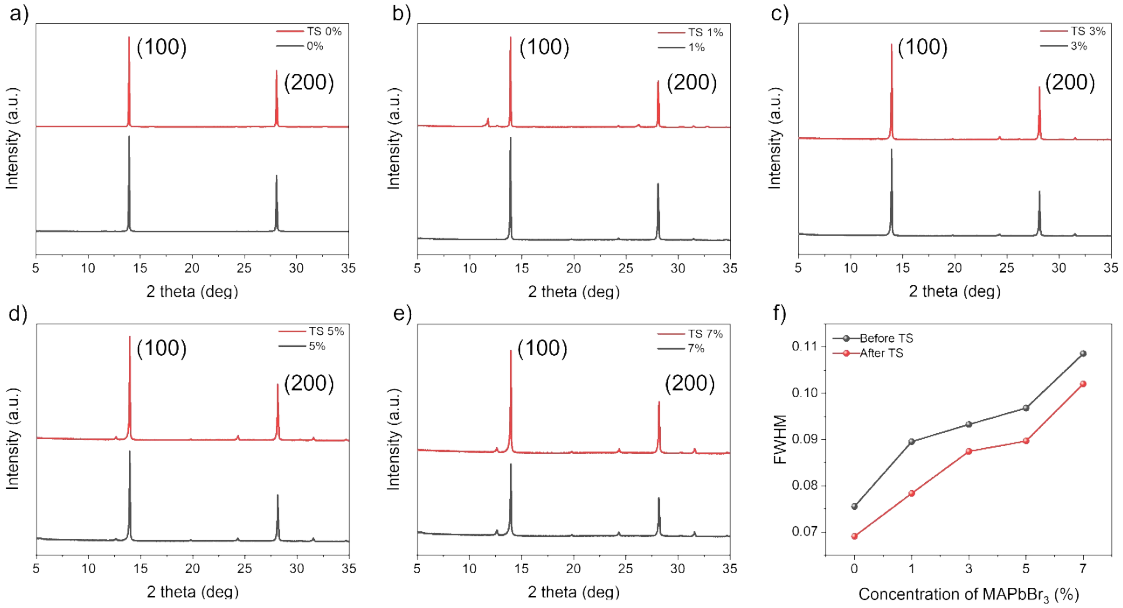

Figure S5. XRD patterns of perovskite films containing 0% (a), 1% (b), 3% (c), 5% (d), and 7% (e) $MAPbBr_3$ before and after TS, along with the corresponding FWHM variations (f).

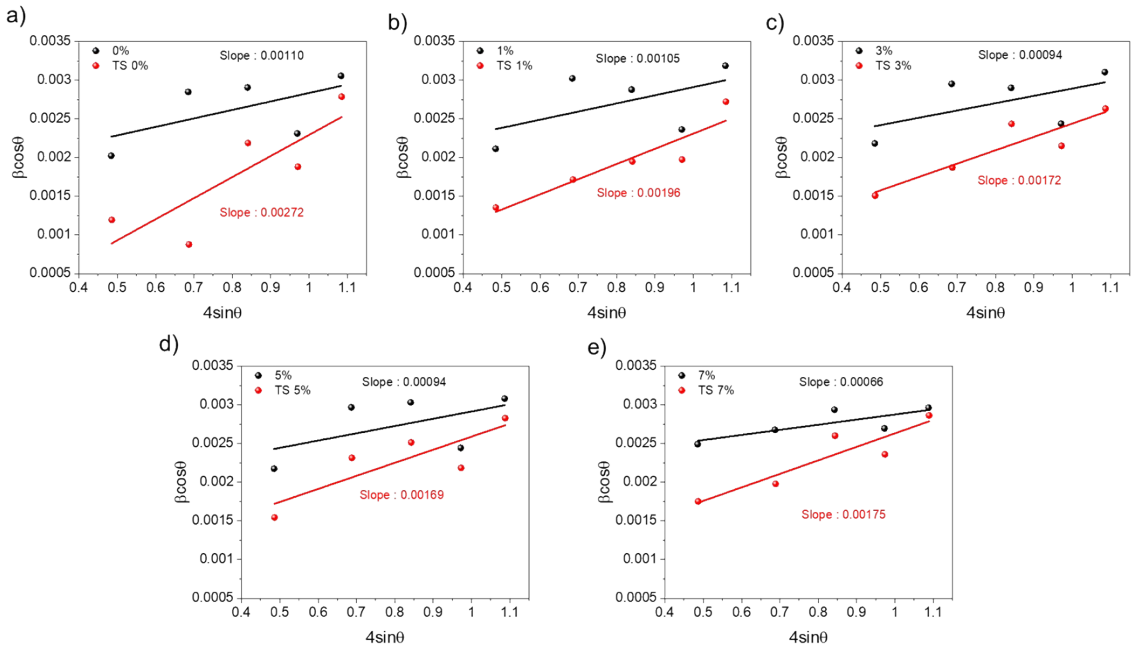

Figure S6. W-H plots for perovskite films with 0% to 7% $MAPbBr_3$ concentrations, measured before and after TS tests.

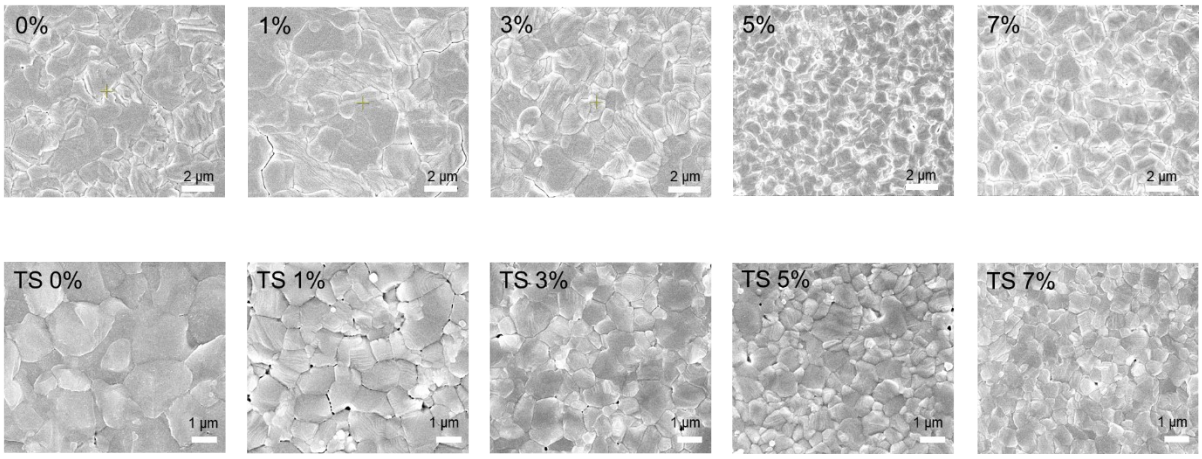

Figure S7. SEM images of perovskite films incorporating $MAPbBr_3$ at concentrations ranging from 0% to 7%, captured both before and after TS.

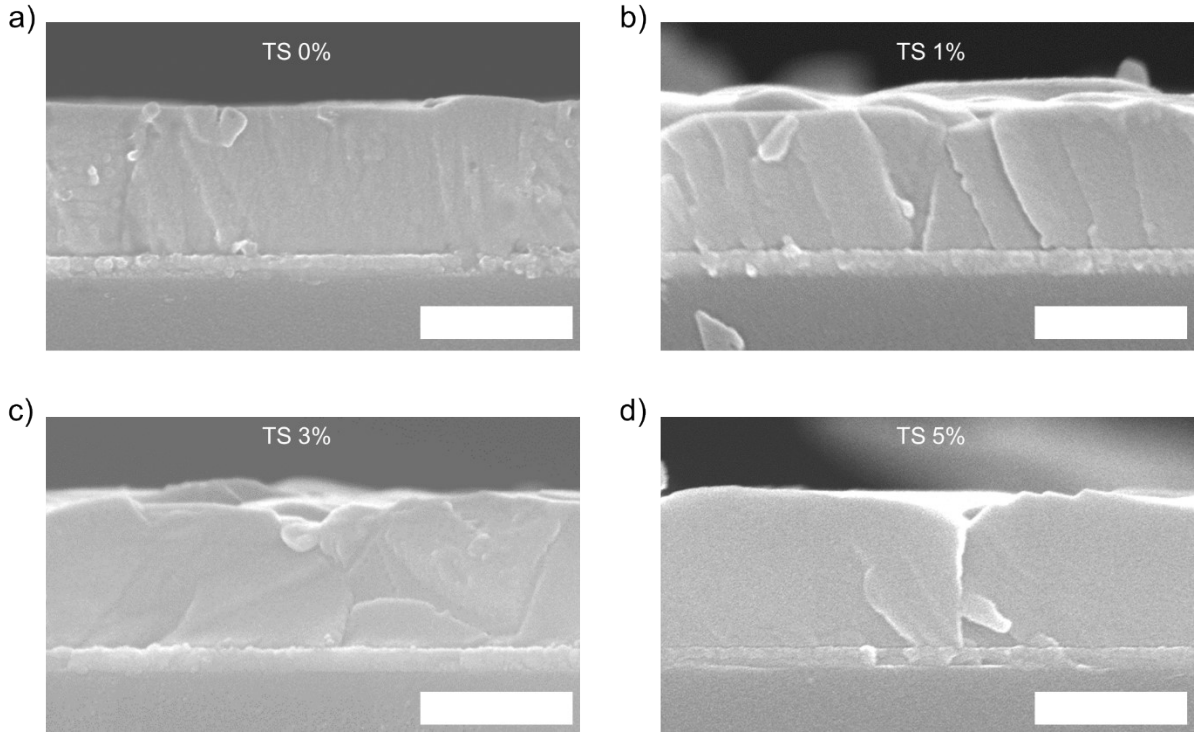

Figure S8. Cross-sectional SEM images of perovskite films after TS test for (a) 0%, (b) 1%, (c) 3%, and (d) 5% $MAPbBr_3$ incorporation. The scale bar corresponds to 500 nm.

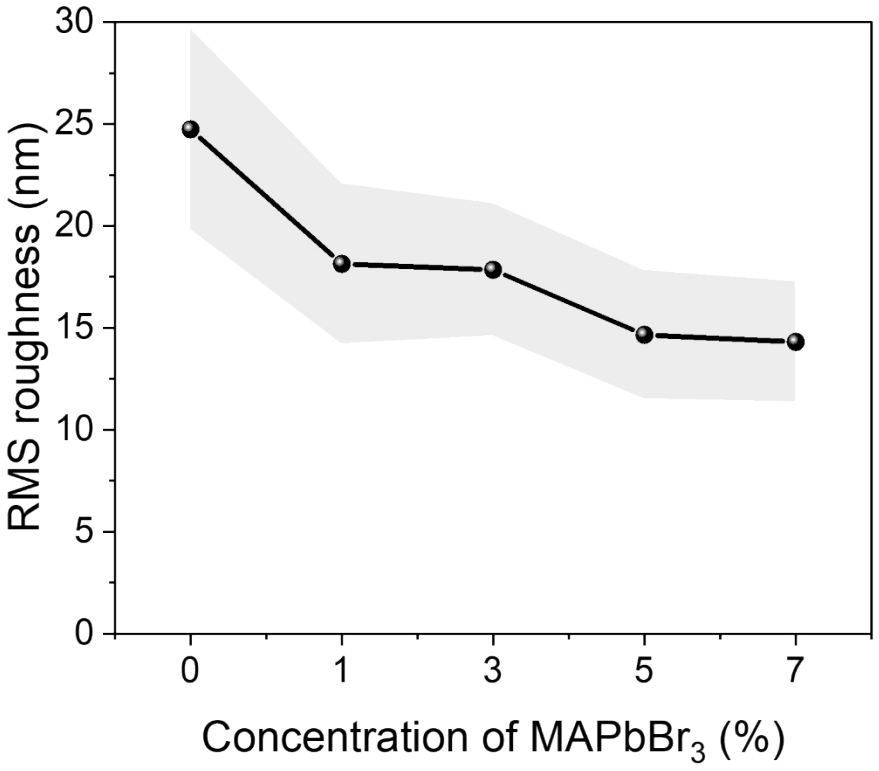

Figure S9. RMS values extracted from AFM topography images before TS.

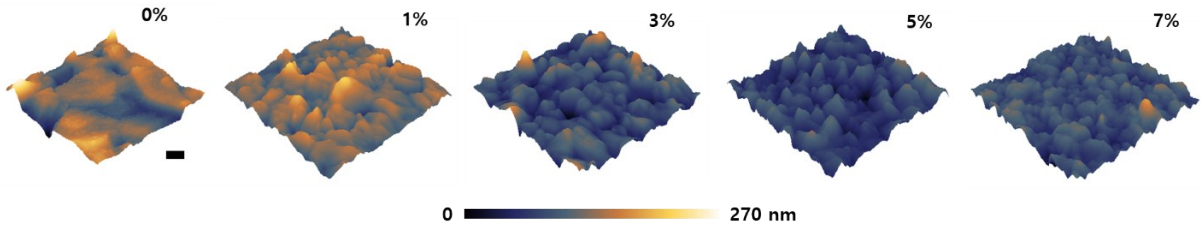

Figure S10. AFM images illustrating the three-dimensional morphology of perovskite films containing $MAPbBr_3$ concentrations from 0% to 7%, measured in the absence of thermal shock. The scale bar corresponds to 500 nm.

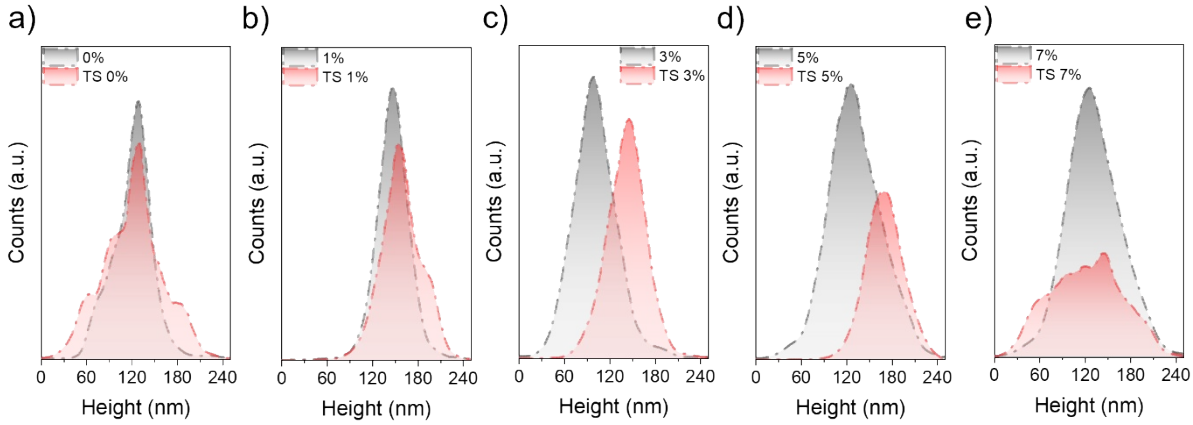

Figure S11. (a)-(e) Histograms of the height distribution of perovskite films before and after TS.

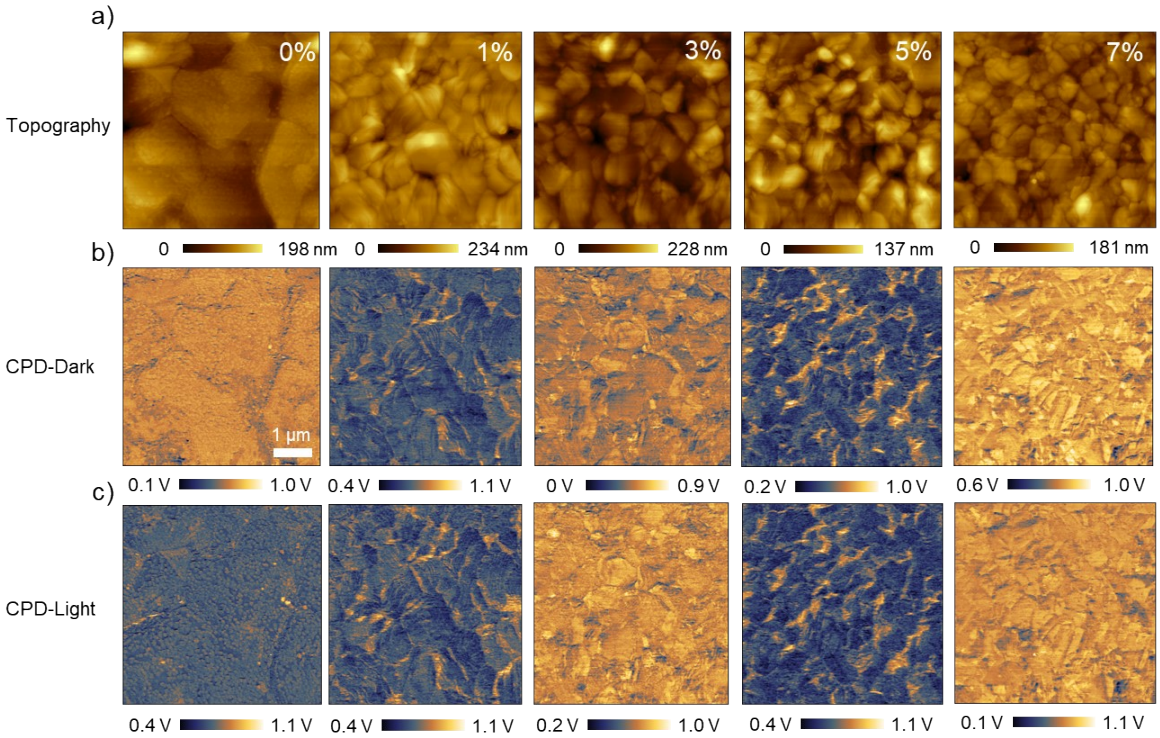

Figure S12. Before TS results of topography and CPD images of perovskite films with $MAPbBr_3$ concentrations ranging from 0% to 7%, measured in the dark and after light exposure.

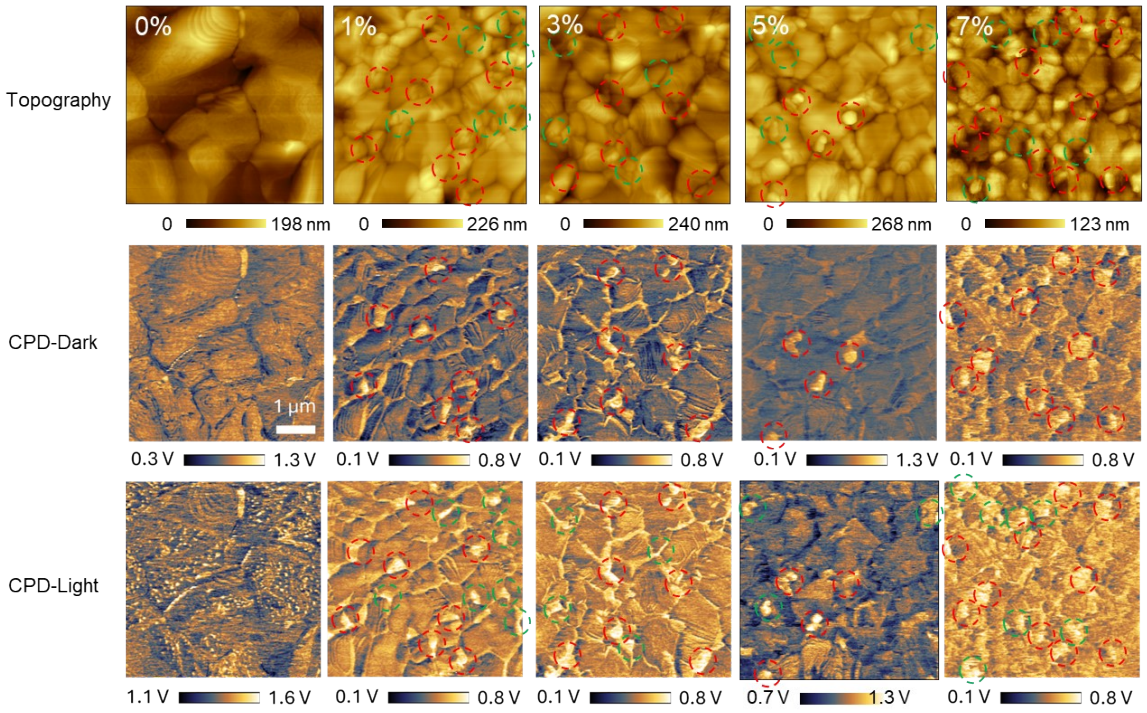

Figure S13. After TS results of topography and CPD images of perovskite films with $MAPbBr_3$ concentrations ranging from 0% to 7%, measured in the dark and after light exposure.

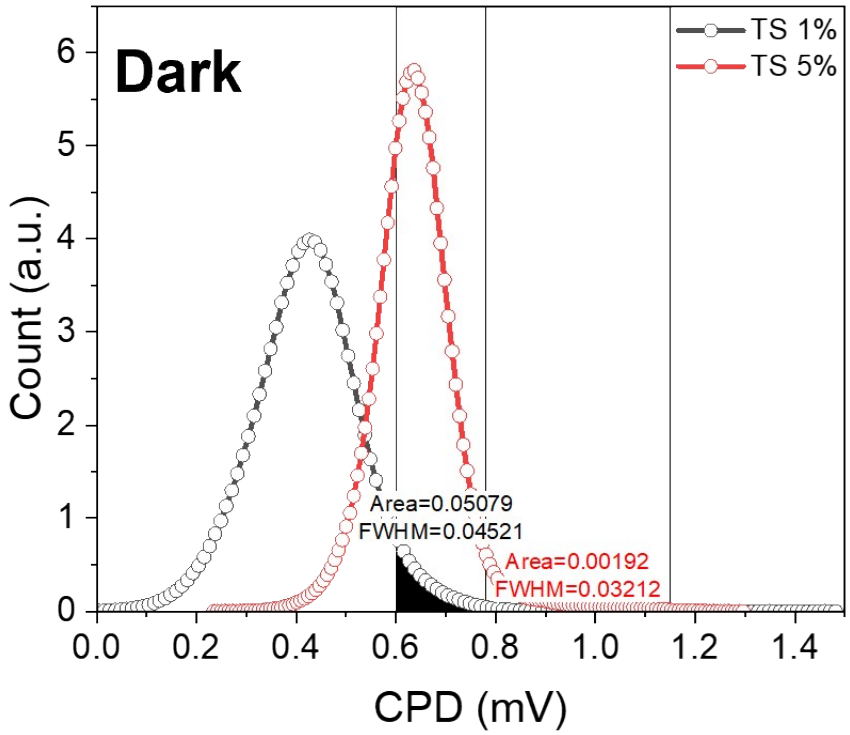

Figure S14. (a) CPD distribution of TS 1% and TS 5% samples under dark conditions.

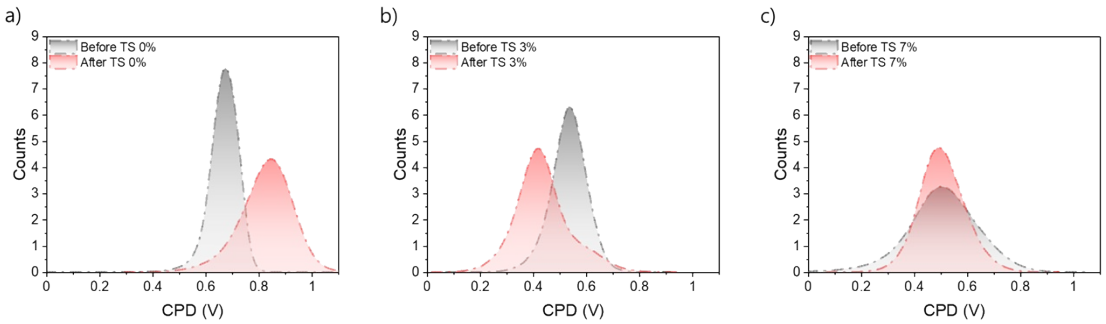

Figure S15. CPD distribution curves for (a) 0%, (b) 3% and (c) 7% of $MAPbBr_3$ samples before and after TS.

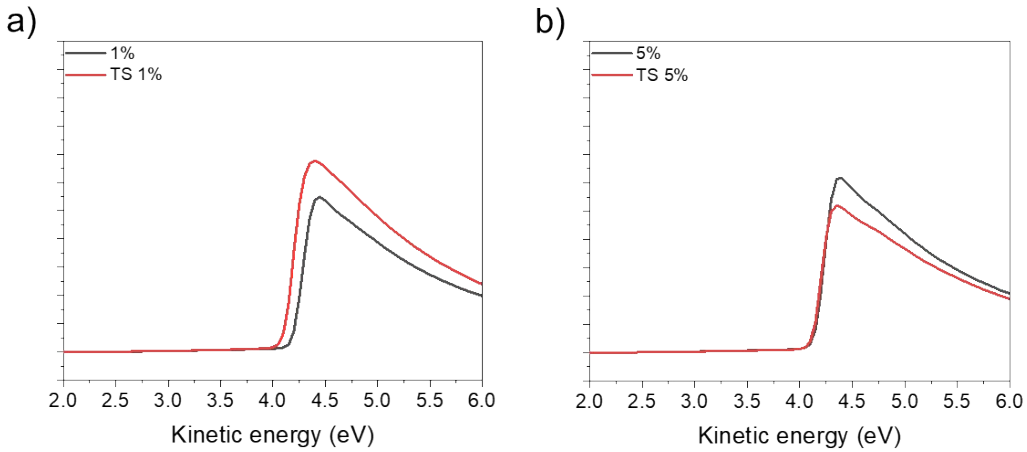

Figure S16. UPS data showing changes in work function before and after TS for perovskite films with $MAPbBr_3$ concentrations of (a) 1% and (b) 5%.

Figure S17. Experimental setup for temperature monitoring under vacuum. A thermocouple was placed on a metal tray and sealed in a polymer vacuum bag to enable real-time temperature measurement within the vacuum environment.

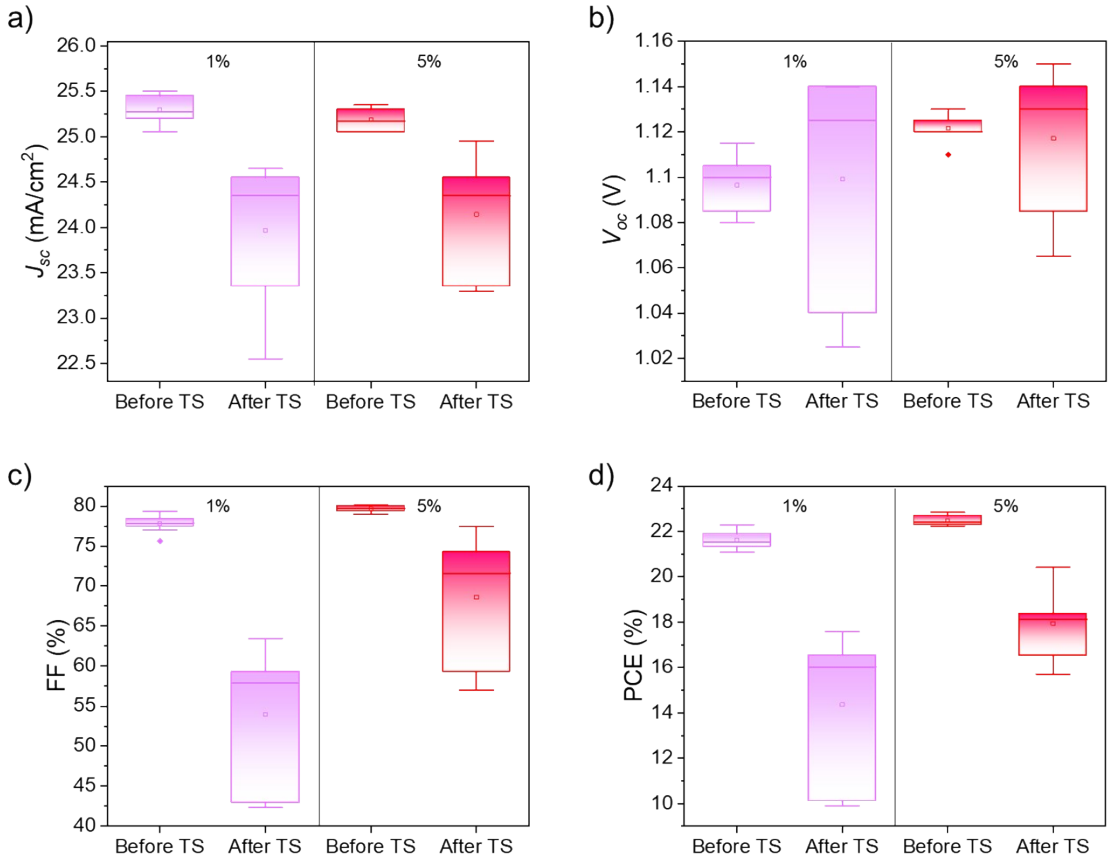

Figure S18. Device performance parameters before and after TS, including (a) J_{SC}, (b) V_{OC}, (c) FF, and (d) PCE for perovskite solar cells.

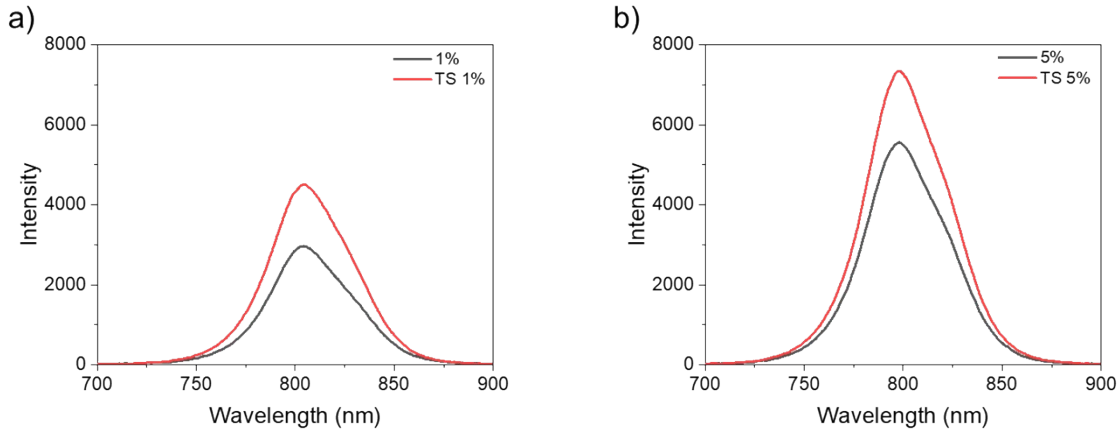

Figure S19. SSPL spectra of (a) 1% and (b) 5% $MAPbBr_3$-doped perovskite films before and after TS treatment.

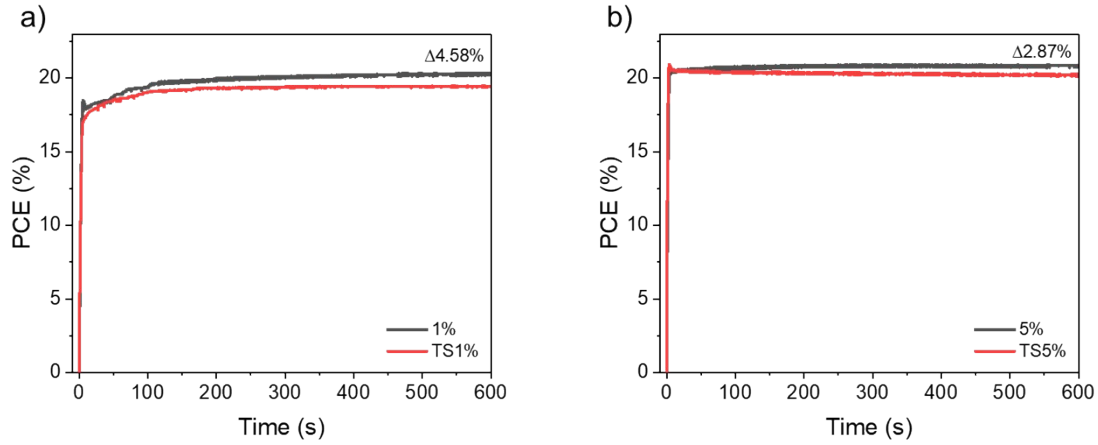

Figure S20. Steady-state power output of 1% and 5% $MAPbBr_3$ devices before and after the TS test.

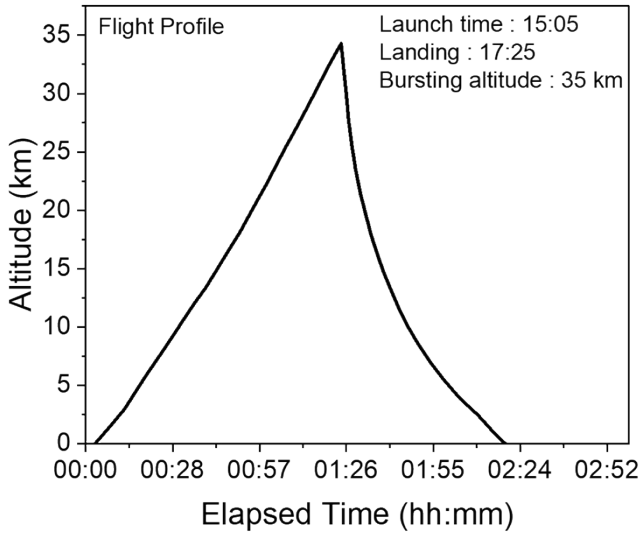

Figure S21. Flight profile of the Pisa HAB test.

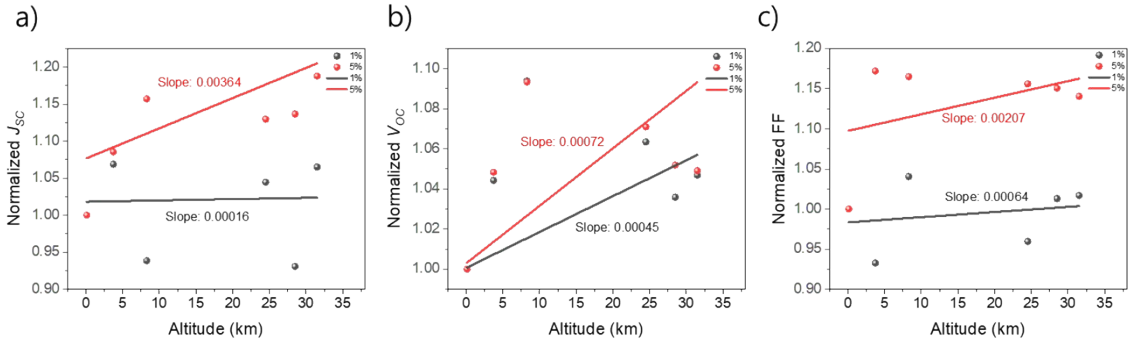

Figure S22. Normalized J_{SC}, V_{OC}, and FF for 1% and 5% $MAPbBr_3$ samples as a function of altitude, including the corresponding slopes with averaged over two devices per composition.

Figure S23. PIB full-cover encapsulation of the perovskite device used in the HAB experiment.

Table S1. Summary comparison of related works and this study

Parameter / Mechanism	**Light cycling *(Shen et al., Nature 2024)*[7]**	**Terrestrial Thermal Cycling (*Chen et al., ACS Energy Lett. 2024*)[8]**	**Space Thermal Shock (This work)**
ΔT range	25~55C	-40~85 °C	±80 °C
Rate of temperature change	Hours-scale (day/night)	Slow/moderate (minutes to hours; IEC 61215 cycle ~2–3 °C/min)	Very fast (16 °C/min or higher in test; much faster than terrestrial)
Cycle duration	24 hours	6 Hours per cycle based on 150 cycles over 37 days	minutes per cycle (orbital transitions between sunlit and eclipse)
Cycle driver	Light on/off with associated temperature swings	Temperature cycling	Temperature shock in vacuum-like conditions
Primary stress origin	Periodic lattice-strain re-formation during cycling	Gradual accumulation of thermal strain across layers	Intrinsic phase instability of $FAPbI_3$ under extreme, rapid ΔT; sensitivity of degradation to $MAPbBr_3$ concentration
Dominant degradation mechanisms	- Strain buildup - deep-trap formation - mild phase distortion	- Grain cracking - interfacial delamination	- Shock-induced α↔δ phase transitions - Grain boundary void formation - Concentration-dependent suppression or acceleration of phase instability
Environmental relevance	Diurnal/light-cycling regime (terrestrial)	Terrestrial PV modules	Harsh space environment of LEO with extreme ΔT and ramp rates

Table S2. In-orbit temperature measurements from satellites in lower LEO.

Satellite or Mission	Temperature (°C)		Altitude (km)	Year	Reference
	Low	High			
AlSat-1N CubeSat	-4	+51	680	2021	[9]
TURKSAT-3USAT CubeSat	-40	+80	680	2021	[10]
Ten-Koh	-40	+20	600	2020	[11]
Ten-Koh	-10	+10	613	2019	[12]
UVSQ-SAT	-20	+40	533	2021	[13]
CubeSat INSPIRE-2	-20	+40	410	2020	[14]
6U CubeSat	-20	+40	400	2022	[15]
MINXSS 3U CubeSat	-30	+60	400	2017	[16]
Super Low Altitude Test Satellite	-10	+20	200	2021	[17]
NOAA-21	-90	+80	824	2022	[18]

Table S3. Orbital periods calculated using Kepler's Third Law and mean thermal transition rates for altitudes from 200 km to 2000 km. Note: Eclipse duration is calculated based on a critical beta angle of 0° (maximum eclipse case). The mean temperature rate represents the mean of the cooling rate (eclipse phase) and heating rate (sunlight phase)

Altitude (km)	Period time (min)	Eclipse Time (min)	Sunlight Time (min)	Temperature Rate at Eclipse (°C/min)	Temperature Rate at Sunlight (°C/min)	Mean Temperature Rate (°C/min)
200	88.35	37.22	51.13	4.30	3.13	3.71
400	92.41	36.05	56.37	4.44	2.84	3.64
600	96.54	35.43	61.11	4.52	2.62	3.57
800	100.72	35.07	65.65	4.56	2.44	3.50
1000	104.97	34.88	70.09	4.59	2.28	3.43
1200	109.27	34.78	74.48	4.60	2.15	3.37
1400	113.63	34.76	78.86	4.60	2.03	3.32
1600	118.04	34.80	83.24	4.60	1.92	3.26
1800	122.51	34.87	87.64	4.59	1.83	3.21
2000	127.04	34.98	92.06	4.57	1.74	3.16

Table S4. Device performance of before and after TS of 1% and 5% samples, showing both best (forward and reverse bias) and average results.

Best device performance						
	Conditions	*Jsc* (mA/cm^2)	*Voc* (V)	FF (%)	PCE (%)	HI (%)
Before TS	1% (forward)	25.50	1.12	79.10	22.93	5.55
	1% (reverse)	25.50	1.10	76.60	21.66	
	5% (forward)	25.40	1.13	80.60	23.23	3.32
	5% (reverse)	25.30	1.12	79.60	22.46	
After TS	1% (forward)	24.70	1.14	66.70	18.82	13.03
	1% (reverse)	24.60	1.10	60.20	16.37	
	5% (forward)	24.90	1.16	73.90	21.29	8.27
	5% (reverse)	25.00	1.14	68.60	19.53	

Table S5. Summary of environmental conditions at around 35 km altitude during the HAB flight.

At 35km altitude	Conditions
Temperature	Decreased the temperature up to -40 °C at around 11 km altitude and increased to around 18 °C at 35 km altitude (**Figure 6c**)
Irradiance	AM0 1370 W/cm^2 (**Figure 6d**)
Pressure	Around 0.55 kPa less than 1% of sea-level pressure[19]
UV light	1km increased -> UV level increased by around 10%[20]

Table S6. Laboratory-measured device performance of 1% and 5% $MAPbBr_3$ samples under AM1.5 prior to the HAB test.

Device Performance of 1% and 5% $MAPbBr_3$ Under AM1.5 Prior to HAB Test				
Conditions	*Jsc* (mA/cm^2)	*Voc* (V)	FF (%)	PCE (%)
1%	22.69	1.09	80.87	19.95
5%	22.81	1.09	80.03	19.95

Table S7. Average device performance for 1% and 5% $MAPbBr_3$ compositions during the HAB flight.

Average device performance of 1% $MAPbBr_3$ under AM0				
Altitude (km)	*Jsc* (mA/cm^2)	*Voc* (V)	FF (%)	PCE (%)
0.14	23.29	1.09	54.21	10.48
3.75	22.92	1.14	52.11	10.28
8.30	21.25	1.21	56.71	10.99
24.50	24.52	1.18	52.70	11.18
28.50	23.86	1.14	54.80	10.91
31.50	24.80	1.15	54.16	11.38

Average device performance of 5% $MAPbBr_3$ under AM0				
Altitude (km)	*Jsc* (mA/cm^2)	*Voc* (V)	FF (%)	PCE (%)
0.14	23.13	1.08	57.39	10.73
3.75	27.04	1.14	61.41	14.35
8.30	28.28	1.20	60.09	15.42
24.50	32.82	1.16	61.12	17.11
28.50	30.42	1.13	59.15	14.97
31.50	31.72	1.14	59.11	15.66

Reference

1. B. Jaeckel, A. Roth, G. Volberg, J. Althaus, G. Kleiss, P. Seidel and M. Beck, 2014.
2. S. J. Clark, M. D. Segall, C. J. Pickard, P. J. Hasnip, M. I. J. Probert, K. Refson and M. C. Payne, *Zeitschrift für Kristallographie - Crystalline Materials*, 2005, **220**, 567-570.
3. J. P. Perdew, K. Burke and M. Ernzerhof, *Physical Review Letters*, 1996, **77**, 3865-3868.
4. A. Tkatchenko and M. Scheffler, *Physical Review Letters*, 2009, **102**, 073005.
5. H. J. Monkhorst and J. D. Pack, *Physical Review B*, 1976, **13**, 5188-5192.
6. M. Gemignani, F. Mancini and S. Marcuccio, 2023.
7. Y. Shen, T. Zhang, G. Xu, J. A. Steele, X. Chen, W. Chen, G. Zheng, J. Li, B. Guo, H. Yang, Y. Wu, X. Lin, T. Alshahrani, W. Yin, J. Zhu, F. Wang, A. Amassian, X. Gao, X. Zhang, F. Gao, Y. Li and Y. Li, *Nature*, 2024, **635**, 882-889.
8. M. Chen, Y. Dong, Y. Zhang, X. Zheng, G. R. McAndrews, Z. Dai, Q. Jiang, S. You, T. Liu, S. P. Harvey, K. Zhu, V. Oliveto, A. Jackson, R. Witteck, L. M. Wheeler, N. P. Padture, P. J. Dyson, M. D. McGehee, M. K. Nazeeruddin, M. C. Beard and J. M. Luther, *ACS Energy Letters*, 2024, **9**, 2582-2589.
9. D. A. Lamb, S. J. C. Irvine, M. A. Baker, C. I. Underwood and S. Mardhani, *Progress in Photovoltaics: Research and Applications*, 2021, **29**, 1000-1007.
10. M. Bulut, *Journal of Thermal Analysis and Calorimetry*, 2021, **143**, 4341-4353.
11. F. Abdullah, K.-i. Okuyama, I. Fajardo and N. Urakami, *Aerospace*, 2020, **7**, 35.
12. I. Fajardo, A. A. Lidtke, S. A. Bendoukha, J. Gonzalez-Llorente, R. Rodríguez, R. Morales, D. Faizullin, M. Matsuoka, N. Urakami, R. Kawauchi, M. Miyazaki, N. Yamagata, K. Hatanaka, F. Abdullah, J. J. Rojas, M. E. Keshk, K. Cosmas, T. Ulambayar, P. Saganti, D. Holland, T. Dachev, S. Tuttle, R. Dudziak and K.-i. Okuyama, *Aerospace*, 2019, **6**, 108.
13. M. Meftah, T. Boutéraon, C. Dufour, A. Hauchecorne, P. Keckhut, A. Finance, S. Bekki, S. Abbaki, E. Bertran, L. Damé, J.-L. Engler, P. Galopeau, P. Gilbert, L. Lapauw, A. Sarkissian, A.-J. Vieau, P. Lacroix, N. Caignard, X. Arrateig, O. Hembise Fanton d'Andon, A. Mangin, J.-P. Carta, F. Boust, M. Mahé and C. Mercier, *Remote Sensing*, 2021, **13**, 1449.
14. I. H. Cairns, C. Charles, A. G. Dempster, J. Funamoto, J. W. Cheong, W. Peacock, J. Lam, B. Osborne, W. Andrew, T. Croston, B. Southwell, R. W. Boswell, A. G. Monger, C. H. Betters, S. G. Leon-Saval, J. Bland-Hawthorn, J. Khachan, X. Wu, S. Manidis, D. Tsifakis and R. Maj, *Space Science Reviews*, 2020, **216**, 40.
15. M. H. B. Azami, N. C. Orger, V. H. Schulz, T. Oshiro, J. R. C. Alarcon, A. Maskey, K. Nakayama, Y. Fukuda, K. Kojima, T. Yamauchi, H. Masui, M. Cho and K. T. M. , *Frontiers in Space Technologies*, 2022, **3**.
16. J. P. Mason, B. Lamprecht, T. N. Woods and C. Downs, *Journal of Thermophysics and Heat Transfer*, 2018, **32**, 237-255.
17. Y. Kimoto, K. Yukumatsu, A. Goto, E. Miyazaki and Y. Tsuchiya, *Acta Astronautica*, 2021, **179**, 695-701.
18. NOAA-STAR, NOAA-21 satellite data, https://ncc.nesdis.noaa.gov/NOAA-21/index.php).
19. U. S. C. o. E. t. t. S. Atmosphere, *US standard atmosphere, 1976*, National Oceanic and Amospheric [sic] Administration, 1976.
20. M. Blumthaler, W. Ambach and R. Ellinger, *Journal of Photochemistry and Photobiology B: Biology*, 1997, **39**, 130-134.